Science Advances
AAAS

Supplementary Materials for

Shape-programmable, deformation-locking, and self-sensing artificial muscle based on liquid crystal elastomer and low–melting point alloy

Haoran Liu, Hongmiao Tian*, Xiangming Li, Xiaoliang Chen, Kai Zhang, Hongyu Shi, Chunhui Wang, Jinyou Shao

*Corresponding author. Email: hmtian@xjtu.edu.cn

Published 18 May 2022, *Sci. Adv.* **8**, eabn5722 (2022)
DOI: 10.1126/sciadv.abn5722

The PDF file includes:

Sections S1 to S5
Figs. S1 to S24
Tables S1 to S3
Legends for movies S1 to S15
References

Other Supplementary Material for this manuscript includes the following:

Movies S1 to S15

Supplementary Text

Section S1. Mathematical Modeling of light-powered multifunctional artificial muscle

In order to understand the deformation mechanism of multifunctional artificial muscle directly, we presented the model of the light-driven multifunctional artificial muscle. To simplify our model, we ideally considered that the parameters of density, specific heat capacity and melting point were stable and their values were unchangeable during the laser heating process.

In the simulation, we regarded the heat source at the irradiating section as a Gaussian heat source, whose energy distribution was defined as follows (42) :

$$q(x,y) = \frac{2\eta P}{\pi w^2} exp\left\{-2\left[\frac{\left(x-\frac{a}{2}\right)^2+(y-b)^2}{w^2}\right]\right\}, \quad (1)$$

where η is the absorption rate of the material to laser, p is laser power, w is set as the radius of laser spot, a set (a/2, b) represents the two-dimensional coordinates of the laser spot center.

The boundary conditions for thermal diffusion in the artificial muscle structure are presented in **Fig. S4**. Meanwhile, we simply assumed the heat energy was wholly absorbed by the multifunctional artificial muscle, i.e., $q_0 = q(x,y)$. q_1 and q_3 were the heat flux due to the thermal convection; q_2 and q_4 were the thermal radiation. Thus, the thermal boundary condition for the surface exposed to light was: $k\nabla T = q_0 - q_1 - q_2$; and the other surface was: $k\nabla T = q_3 + q_4$, with k being the thermal conductivity of LCE, ∇T being the temperature gradient along the normal direction of surface.

The thermal convection over the two surfaces of multifunctional artificial muscle was assumed to satisfy the nature convection condition. The heat flux of q_1 and q_3 in the irradiated and non-irradiated surfaces was represented as: $q_1 = h_c(T_{upper} - T_{room})$ and $q_3 = h_c(T_{lower} - T_{room})$, respectively, where T_{upper} and T_{lower} were the temperature of upper surface and lower surface, respectively; T_{room} represented room temperature; h_c was the convection coefficient, which was estimated to be 20 $Wm^{-2}K^{-1}$. The upper and lower surfaces of multifunctional artificial muscle also radiated heat energy into the ambient environment, which were governed by q_2 and q_4 in upper surface and lower surface, respectively. The radiation loss was assumed to satisfy the Stefan-Boltzmann law. Thus, the heat fluxes were given by: $q_2 = \varepsilon\sigma(T_{upper}^4 - T_{room}^4)$ and $q_4 = \varepsilon\sigma(T_{lower}^4 - T_{room}^4)$ over the upper and lower surfaces. We also assumed the nut-brown artificial muscle was a black body and set the emissivity as: $\varepsilon = 1$. The Stefan-Boltzmann constant was set as: $\sigma = 5.67\times10^{-8}$ $Wm^{-2}K^{-4}$.

Based on theory of heat conduction, the temperature field of the artificial muscle structure (i.e., inner LMPA rod and outside tubular LCE): $T = T(x,y,t)$ was governed by the heat conduction equation:

$$\rho c\frac{\partial T}{\partial t} - k\nabla^2 T = 0, \quad (2)$$

where ρ is mass density, c is specific heat capacity, k is the thermal conductivity and ∇^2 denotes Laplace operator.

In the model, the heat transfer with steady heat source flowing through a multi-layered structures caused the temperature change of multifunctional artificial muscle. Basically, the surface heat of LCE at irradiating section conducted inward by heat conduction. When the heat reached the LMPA surface, it continued to diffuse in LMPA by heat conduction due to the temperature difference. The conducted heat could trigger the rise of temperature in LMPA, and LMPA would melt when the temperature exceeds the melting point of LMPA. According to the heat conduction equation (2) mentioned above, the temperature distribution of multifunctional artificial muscle and inner LMPA is presented in **Figs. S5** and **S6**, respectively.

The main parameters of LCE and LMPA in simulation can be seen in **Table S1**. In order to achieve the liquid-solid transformation of LMPA, we mainly set temperature-dependent Young's modulus in simulation, which can be seen in **Table S2**. The values of Young's Modulus and Poisson Ratio of LCE adopted in the numerical simulations can be seen in **Table S3**.

Section S2. Mechanical analysis of bending deformation of multifunctional artificial muscle

In the simulation, we could observe that the LMPA at the laser irradiation section melted when the temperature exceeded the melting point of LMPA. In order to study the deformation mechanism, we built the model as shown in **Fig. S7**. When the laser was irradiated on the surface of LCE, the contracting force (*F'*) in the LCE generated along with the macroscopic shrinkage deformation. The compressive force *F* would be applied on the surface of LMPA rod by the static friction between two surfaces. Here, we assumed that the value of *F* was equal to the value of *F'* (i.e., *F* = *F'*). The joule heat generated at the surface of LCE would melt the LMPA under the LCE film via thermal conduction. The multifunctional artificial muscle generated bending deformation when the un-melted LMPA at the irradiating section would not bear the action of *F*.

Here, we considered the first case: the melting cross-sectional area of LMPA was smaller than the un-melted cross-sectional area at the irradiating section. The geometric relationship of cross section of LMPA rod could be seen in **Fig. S8.** In this case, the melting section, we assumed, was bow-shaped sturcture. Here, β was the semicircular angle of a bow-shaped section, *R* was the radius of LMPA rod. Thus, The distance between the center point of cross section of LMPA rod and centroid of bow-shaped structure was expressed as (43):

$$L' = \frac{4Rsin^3\beta}{3(2\beta - sin2\beta)}. \tag{3}$$

The moment of inertia of bow-shaped structure was described as follows (43, 61):

$$I_x = \frac{1}{4}R^4\beta + \frac{1}{2}R^4 cos\beta sin^3\beta - \frac{1}{4}R^4 cos\beta sin\beta - \frac{4R^4 sin^6\beta}{9(\beta - cos\beta sin\beta)}. \tag{4}$$

The moment of inertia of cross section of LMPA rod was given by:

$$I_x' = \frac{1}{4}\pi R^4. \tag{5}$$

The ordinate value of the centroid of un-melted cross section of LMPA rod was represented as:

$$y_c = \frac{S_x}{A} = \frac{0 - \frac{R^2(2\beta - sin2\beta)}{2} \cdot \frac{4Rsin^3\beta}{3(2\beta - sin2\beta)}}{\pi R^2 - \frac{R^2(2\beta - sin2\beta)}{2}} = -\frac{\frac{4}{3}Rsin^3\beta}{2\pi - 2\beta + sin2\beta}. \tag{6}$$

The area of cross section of LMPA rod was expressed as:

$$A_1 = \pi R^2. \tag{7}$$

The area of melted bow-shaped cross section was described by using:

$$A_2 = \frac{R^2(2\beta - sin2\beta)}{2}. \tag{8}$$

Thus, the cross-sectional area of un-melted LMPA rod was given by:

$$A = A_1 - A_2 = \pi R^2 - \frac{R^2(2\beta - sin2\beta)}{2}. \tag{9}$$

Hence, the moment of inertia of un-melted cross section of LMPA rod was calculated by the following equation:

$$\begin{aligned} I_{xc} &= I_x + A_1 y_c^2 - I_x' - A_2(L' - y_c)^2 \\ &= \frac{\pi(2R)^4}{64} + \pi R^2 \left(-\frac{\frac{4}{3}Rsin^3\beta}{2\pi - 2\beta + sin2\beta} \right)^2 \\ &\quad - \left[\frac{1}{4}R^4\beta + \frac{1}{2}R^4 cos\beta sin^3\beta - \frac{1}{4}R^4 cos\beta sin\beta - \frac{4R^4 sin^6\beta}{9(\beta - cos\beta sin\beta)} \right] \\ &\quad - \frac{R^2(2\beta - sin2\beta)}{2} \left[\frac{4Rsin^3\beta}{3(2\beta - sin2\beta)} + \frac{\frac{4}{3}Rsin^3\beta}{2\pi - 2\beta + sin2\beta} \right]^2 \end{aligned}$$

$$= \frac{\left\{\begin{array}{c} \frac{9}{4}\pi R^4(2\beta - sin2\beta)(2\pi - 2\beta + sin2\beta)^2 + 16\pi R^4 sin^6\beta(2\beta - sin2\beta) - \\ \left[9(2\beta - sin2\beta)\left(\frac{1}{4}R^4\beta + \frac{1}{2}R^4 cos\beta sin^3\beta - \frac{1}{4}R^4 cos\beta sin\beta\right)\right](2\pi - 2\beta + sin2\beta)^2 - \\ -8R^4 sin^6\beta \end{array}\right\}}{9(2\beta - sin2\beta)(2\pi - 2\beta + sin2\beta)^2}$$

$$= \frac{\left\{\begin{array}{c} (2\pi - 2\beta + sin2\beta)^2\left[(2\beta - sin2\beta)\cdot\frac{9}{16}R^4(4\pi - 4\beta + sin4\beta) + 8R^4 sin^6\beta\right] - \\ 16\pi R^4 sin^6\beta(2\pi - 2\beta + sin2\beta) \end{array}\right\}}{9(2\beta - sin2\beta)(2\pi - 2\beta + sin2\beta)^2}$$

$$= \frac{\left\{\begin{array}{c} (2\pi-2\beta+sin2\beta)\left[(2\beta-sin2\beta)\cdot\frac{9}{16}R^4(4\pi-4\beta+sin4\beta)+8R^4sin^6\beta\right]- \\ 16\pi R^4 sin^6\beta \end{array}\right\}}{9(2\beta-sin2\beta)(2\pi-2\beta+sin2\beta)}. \quad (10)$$

The distance between the centroid of bow-shaped structure and solid-liquid boundary of it was obtained by:

$$y_{max} = Rcos\beta - y_c = Rcos\beta + \frac{\frac{4}{3}Rsin^3\beta}{2\pi-2\beta+sin2\beta}. \quad (11)$$

The bending moment of LMPA rod triggered by actuating force of LCE tubular actuator was given by:

$$M = F(R - y_c) = F(R + \frac{\frac{4}{3}Rsin^3\beta}{2\pi-2\beta+sin2\beta}). \quad (12)$$

Hence, the stress of LMPA rod at bending moment should meet the following condition:

$$\sigma_L = \frac{F}{A} + \frac{My_{max}}{I_{xc}} \geq [\sigma_L]. \quad (13)$$

Thus, the relationship between actuating force of the LCE and the angle of the melted area was be rewritten as:

$$\frac{1}{F} \leq \frac{2}{R^2(2\pi-2\beta+sin2\beta)[\sigma_L]}\left\{1 + \frac{\frac{9}{2}(2\beta-sin2\beta)[cos\beta(2\pi-2\beta+sin2\beta)^2+\frac{4}{3}sin^3\beta(1+cos\beta)(2\pi-2\beta+sin2\beta)+\frac{16}{9}sin^6\beta]}{(2\pi-2\beta+sin2\beta)\left[\frac{9}{16}(2\beta-sin2\beta)(4\pi-4\beta+sin4\beta)+8sin^6\beta\right]-16\pi sin^6\beta}\right\}. \quad (14)$$

Another case should not be ignored: the melting cross-sectional area of LMPA was larger than the un-melted cross-sectional area at the irradiating section, as shown in **Fig. S9**. The cross section of un-melted LMPA was nearly approximated as a bow-shaped structure. In **Fig. S9**, α was the semicircular angle of a bow-shaped section, R was the radius of LMPA rod. Thus, the distance between the center point of cross section of LMPA rod and the centroid of bow-shaped structure was expressed as (*43*):

$$L' = \frac{4Rsin^3\alpha}{3(2\alpha-sin2\alpha)}. \quad (15)$$

The area of bow-shaped structure was given by:

$$A = \frac{R^2(2\alpha-sin2\alpha)}{2}. \quad (16)$$

The bending moment of LMPA rod triggered by actuating force of LCE tubular actuator was expressed as:

$$M = FL = F[\frac{4Rsin^3\alpha}{3(2\alpha-sin2\alpha)} + R]. \quad (17)$$

The moment of inertia of bow-shaped structure was given by:(*2, 3*)

$$I_x = \frac{1}{4}R^4\alpha + \frac{1}{2}R^4 cos\alpha sin^3\alpha - \frac{1}{4}R^4 cos\alpha sin\alpha - \frac{4R^4 sin^6\alpha}{9(\alpha-cos\alpha sin\alpha)}. \quad (18)$$

Meanwhile, the distance between arch centroid and solid-liquid boundary of bow-shaped structure was expressed as:

$$y_{max} = L' - Rcos\alpha = \frac{4Rsin^3\alpha}{3(2\alpha - sin2\alpha)} - Rcos\alpha. \quad (19)$$

The multifunctional artificial muscle would generate bending deformation when the stress σ_L of LMPA rod at bending moment was larger than the maximum allowable compressive stress $[\sigma_L]$, i.e.:

$$\sigma_L = \frac{F}{A} + \frac{My_{max}}{I_x} \geq [\sigma_L]. \quad (20)$$

Thus, the relationship between the actuating force of the LCE and the angle of the un-melted area (i.e., cross section of bow-shaped structure) was rewritten as:

$$\frac{1}{F} \leq \frac{2}{R^2(2\alpha - sin2\alpha)[\sigma_L]}\left[1 + \frac{4sin^6\alpha + 3sin^3\alpha(1-cos\alpha)(2\alpha - sin2\alpha) - \frac{9}{4}cos\alpha(2\alpha - sin2\alpha)^2}{\frac{9}{32}(2\alpha - sin2\alpha)(4\alpha - sin4\alpha) - 4sin^6\alpha}\right]. \quad (21)$$

Section S3. Deformation recovery of multifunctional artificial muscle.

In the experiment, we vertically fixed an artificial muscle (length: 50 mm) on a clamp. Then a laser beam with an irradiating power of 1.3 W was applied on one side of artificial muscle at 0 s. After irradiated for about few seconds, the artificial muscle generated bending deformation and reached the maximum bending angle at 8 s. Then the artificial muscle sustained the maximum bending angle without any recovery. At 16 s, two laser beams were applied on both sides of bending position of artificial muscle. By alternately or simultaneously irradiating the bending position, the artificial muscle recovered to upright state again at 32 s. The whole deformation process can be seen in **Fig. S20** or **Movie S14.**

Section S4. Comparison of bending stiffness and load bearing capacity of multifunctional artificial muscle

A structure's stiffness usually indicates its ability to maintain its shape under external load. To facilitate the evaluation of bending stiffness, we use the slope of force–displacement curve to define the stiffness *k* of multifunctional artificial muscle. The equation of bending stiffness can be seen as follow (44):

$$k = \frac{F}{\delta}, \quad (22)$$

where *F* is the applied external force and δ is the corresponding displacement caused by the external force. In the experiment, one end of the artificial muscle was horizontally fixed and the other end was free. Meanwhile, *F* was applied on the free end of multifunctional artificial muscle with its direction perpendicular to the longitudinal direction of multifunctional artificial muscle.

As shown in the inset of **Fig. S17A**, the force sensor pressed the end of the LCE tubular actuator at a constant speed of 1 mm/min until it was moved downwards about 2 mm, then the force-displacement relationship of the artificial muscle was recorded. Output force *F* for the three different diameters (2 mm, 2.4 mm, and 2.9 mm) linearly increased as the displacement increased from 0 mm to 2 mm. At a displacement of 2 mm, the force dramatically increased from 3 mN to 15 mN when the diameter of the LCE tubular actuator increased from 2 mm to 2.9 mm.

Fig. S17B shows the output force of the multifunctional artificial muscle with different outside diameters (2 mm, 2.4 mm, and 2.9 mm), which was recorded by a force sensor that moved downward with a uniform speed of 1 mm/min. The force of the multifunctional artificial muscle increased from 0 mN without delay. The output force of the multifunctional artificial muscle increased as the displacement increased from 0 mm to 2 mm. With the increase of displacement, the force–displacement curve of the artificial muscle became evidently nonlinear. At a displacement of 2 mm, the force dramatically increased from 284 mN to 1288 mN when the diameter of the multifunctional artificial muscle increased from 2 mm to 2.9 mm.

Fig. S17C compares the bending stiffness of multifunctional artificial muscle and LCE tubular actuator with different radiuses. Bending stiffness *k* under radius of 2 mm, 2.4 mm, and 2.9 mm was 3 mN/mm, 6 mN/mm, and 14.6 mN/mm, respectively, for LCE tubular actuator and 200

mN/mm, 474 mN/mm, and 1086 mN/mm, respectively, for multifunctional artificial muscle. The bending stiffness of the multifunctional artificial muscle was improved about 133-fold with a diameter of 2 mm, 158-fold with a diameter of 2.4 mm, and 155-fold with a diameter of 2.9 mm. Thus, increasing the diameter of the LCE and embedding high stiffness LMPA can effectively improve the bending stiffness of the artificial muscle.

A comparison of load-bearing force of the multifunctional artificial muscle and LCE tubular actuator with different diameters is presented in **Fig. S17D**. Load-bearing force *F* under the radius of 2 mm, 2.4 mm, and 2.9 mm was 1.5 mN, 3 mN, and 7 mN, respectively, for the LCE tubular actuator and 284 mN, 494 mN, 1266 mN, respectively, for the multifunctional artificial muscle. Hence, the load-bearing force can be significantly improved by increasing the diameter and embedding high stiffness LMPA in LCE tubular actuator.

Section S5. The test of resistance change of LMPA under different temperatures.

In order to study the influence of temperature on resistance of LMPA, we prepared a sample by encapsulating a LMPA rod (length: 30 mm, diameter: 1 mm) in fluororesin. Then a prepared sample was placed on a hot plate, whose temperature was increased from 40 ℃ to 150 ℃ with an interval of 10 ℃. Thus, the resistance of sample in thermal equilibrium state was obtained by precision source/measure unit (Keysight B2912A). Here, we ignored the influence of thermal expand coefficient of fluoroethylene resin on resistance of LMPA for a low thermal coefficient of expansion. As shown in **Fig S22A**, the resistance change ($\Delta r/r$) increased from zero to 6.7% by increasing the temperature from 40 ℃ to 150 ℃. If we shortened heating length of sample, the resistance change of the sample would decreased. Particularly, if the heating length of the sample was shortened to 2 mm, i.e., one fifteenth of the original length, the resistance change ($\Delta R/R$) of the sample under ideal condition would also be one-fifteenth of the original value (**Fig. S22B**) based on the equation of

$$\Delta R/R = \frac{\left[\frac{1}{15}\left(\frac{\Delta r}{r}\right)+\frac{14}{15}\cdot 0\right]}{1} = \frac{1}{15}(\Delta r/r). \quad (23)$$

In experiments, the laser spot diameter was about 2 mm. Thus, we could roughly estimate the resistance change of multifunctional artificial muscle based on the data presented in **Fig. S22B**. According to the data, resistance change of multifunctional artificial muscle was below 0.5% whether it was owing to temperature or phase transition of LMPA.

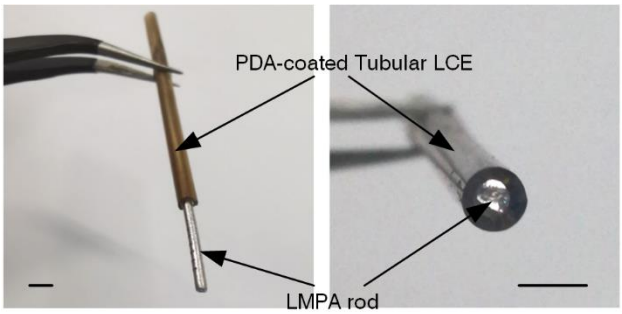

Fig. S1. Structure of multifunctional artificial muscle. A prefabricated LMPA rod (melting point is 100 ℃) was embedded in PDA-coated LCE-based tubular actuator (scale bars: 2.5 mm).

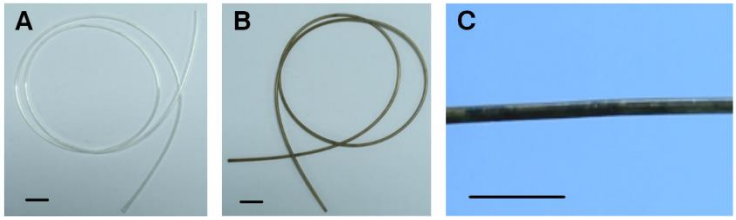

Fig. S2. Sample of tubular LCE, PDA-coated tubular LCE, and multifunctional artificial muscle in A, B, and C, respectively. In (A-C), the scale bars are 15 mm.

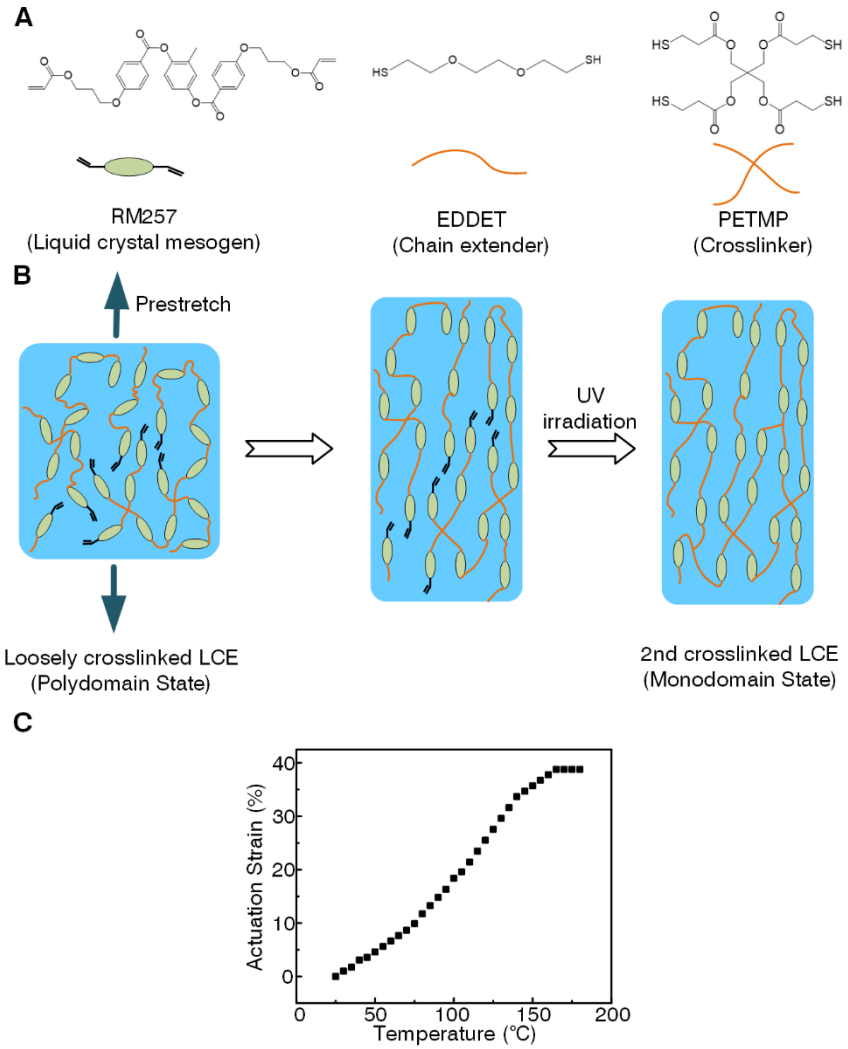

Fig. S3. Chemical component, fabrication process, and actuation performance of an LCE film. (**A**) RM257 was the liquid crystal mesogen, EDDET was the chain extender, and PETMP was the crosslinker. (**B**) Monodomain LCE was obtained by stretching loosely crosslinked LCE to align liquid crystal mesogen and then exposed under UV irradiation to stimulate the second crosslinked process. (**C**) The actuation strain of LCE under different temperatures (the length of 2nd crosslinked LCE test sample was five times length of it in polydomain state). To quantitatively characterize the actuation of the LCE film, we defined the actuation strain along length direction as $\varepsilon = (L - l)/L \times 100\%$, where L and l were the lengths of LCE film in the initial and actuated states, respectively.

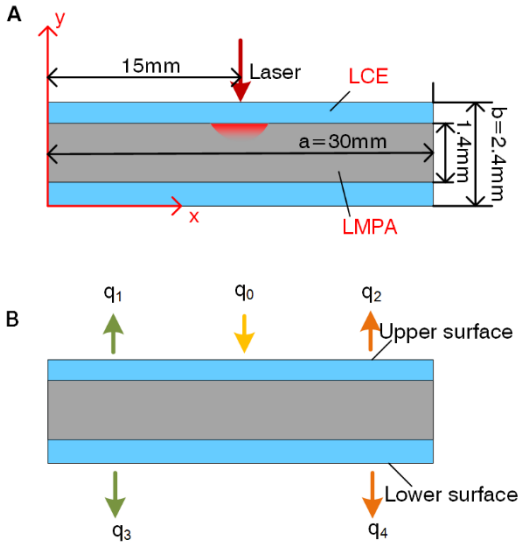

Fig. S4. Two-dimensional model and heat boundary conditions of multifunctional artificial muscle in simulation. (**A**) The two-dimensional model of multifunctional artificial muscle adopted in simulation. The laser spot was applied on the middle of upper surface. The length (a) of the model was 30 mm; the inner diameter and outside diameter (b) of LCE were 1.4 mm and 2.4 mm, respectively; the diameter of LMPA was 1.4 mm. (**B**) Associated heat fluxes at the upper surface and lower surface. q_0 was the heat flux converted from the incoming light; q_1 and q_3 were the heat fluxes due to thermal convection; q_2 and q_4 were the thermal radiation.

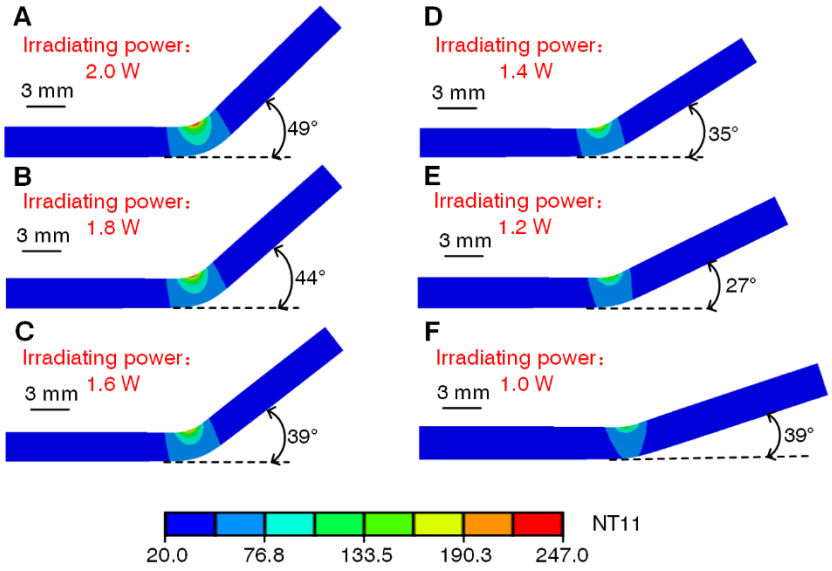

Fig. S5. Influence of irradiating power on the temperature distribution of multifunctional artificial muscle in simulation. (**A-F**) Temperature distribution of artificial muscle under different irradiating powers in simulation.

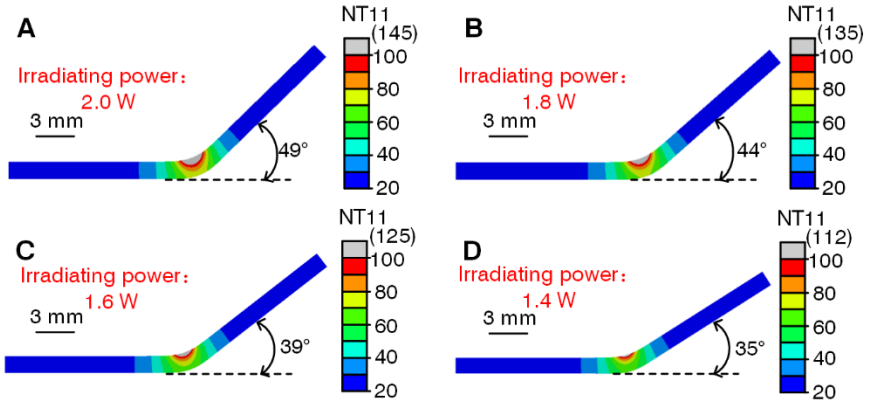

Fig. S6. Influence of irradiating power on the size of melting section of LMPA. (**A-D**) Temperature distribution of rod-like LMPA by concealing PDA-coated LCE tubular actuator in simulation. The grey color represents the temperature above 100 ℃, which also means the LMPA being in melting state.

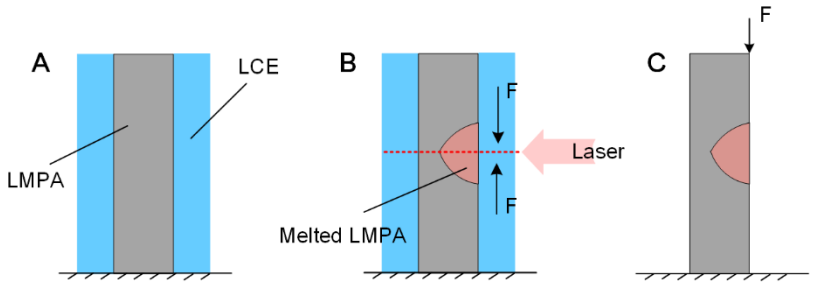

Fig. S7. Deformation mechanism of multifunctional artificial muscle. (**A**) The structure of multifunctional artificial muscle. (**B**) The structure change and actuating force of multifunctional artificial muscle under laser irradiation. (**C**) The compressive force *F* applied on the surface of LMPA via static friction. Before deformation, Actuating force in LCE induced by laser irradiation was applied on surface of LMPA via the function of static friction. Meanwhile, the heat generated on the surface of LCE also heated the LMPA at the laser irradiating section via heat conduction. Thus, the LMPA would melt when the temperature exceeded its melting point. With the increase of the actuating force and melting section, the multifunctional artificial muscle was easy to generate bending deformation.

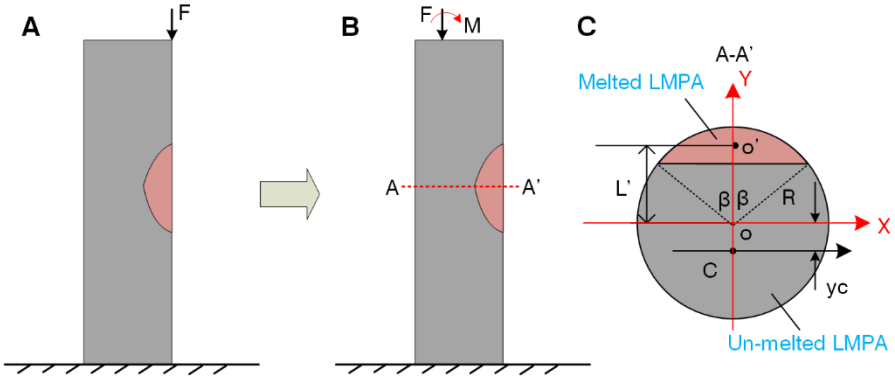

Fig. S8. Schematic illustration of LMPA rod with small melted area at laser irradiation section. (**A**) The actuating force of LCE was applied on surface of LMPA by the function of static friction. (**B**) The equivalent form of (A). The direction of *F* was through the centroid of cross section of un-melted LMPA at A-A'. (**C**) The cross section of LMPA rod at A-A'.

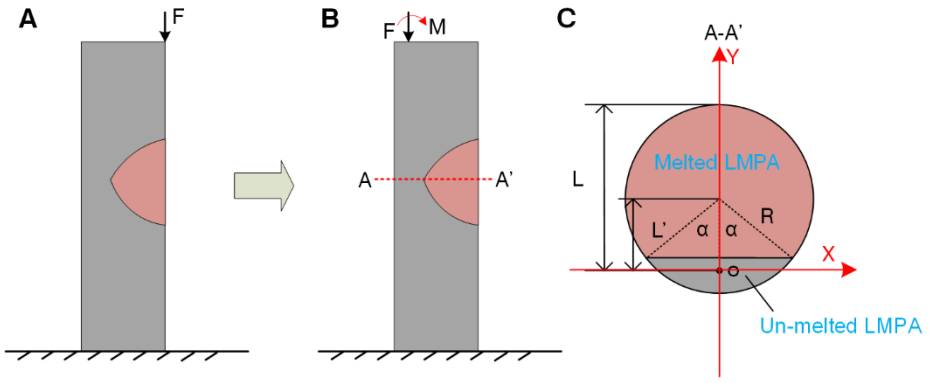

Fig. S9. Schematic illustration of LMPA rod with large melted area at laser irradiation section. (**A**) The actuating force of LCE was applied on surface of LMPA by the function of static friction. (**B**) The equivalent form of (A). The direction of *F* was through the centroid of cross section of un-melted LMPA at A-A'. (**C**) The cross section of LMPA rod at A-A'.

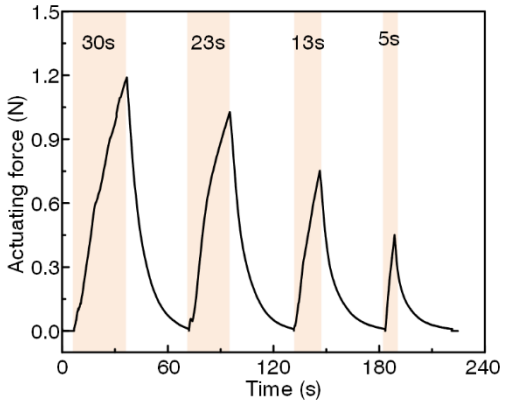

Fig. S10. Influence of irradiating time on actuating force of PDA-coated LCE-based tubular actuator. In the test, two ends of PDA-coated LCE tubular actuator were fixed on testing machine. Laser spot was applied on the middle of PDA-coated LCE tubular actuator. Meanwhile, we kept the laser power unchangeable, and only changed the irradiating time from 5 to 30 s.

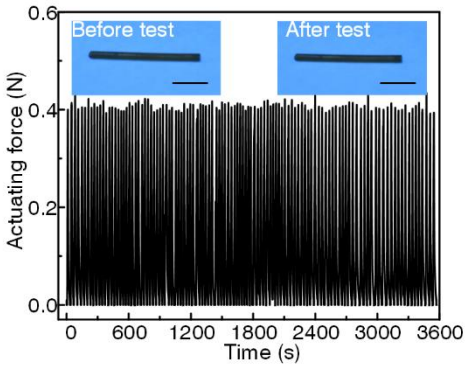

Fig. S11. Surface of PDA-coated LCE-based tubular actuator before/after irradiation. Actuating force cycle test of PDA-coated LCE tubular actuator under the laser irradiation of 1.0 W (inner diameter: 1.4 mm, outsider diameter: 2.4 mm) with a testing time of 3600 s. The inset shows the surface of PDA-coated LCE tubular actuator before and after cycle test (scale bars: 10 mm).

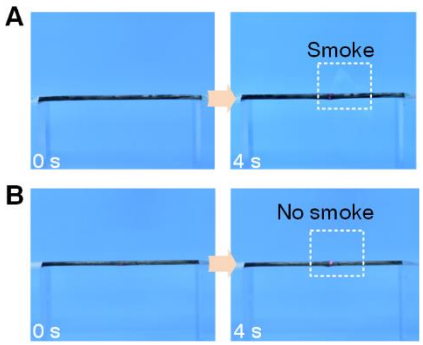

Fig. S12. Comparison of tubular LCE coated with thick PDA layer and that with thin PDA layer under same irradiating power (1.8 W). (**A**) Tubular LCE coated with thick PDA layer easily generating smoking or scorch (here, the samples were immersed in dopamine/Tris base buffer solution for about a week). (**B**) Tubular LCE coated with thin PDA layer hardly generating smoking or scorch. (here, the samples were immersed in dopamine/Tris base buffer solution for about 24 h). In the tests, the samples of PDA-coated tubular LCE were suspended between two objects, and two ends of samples were fixed on the two objects.

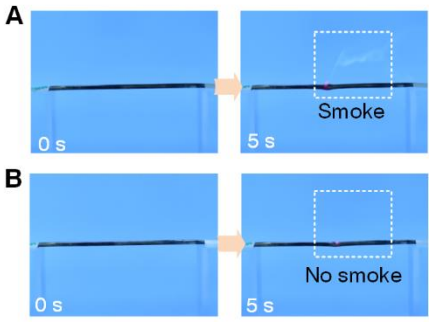

Fig. S13. Influence of irradiating power on tubular LCE coated with thick PDA layer (the samples were immersed in dopamine/Tris base buffer solution for about a week). (**A**) Tubular LCE coated with thick PDA layer easily generating smoking or scorch under a high irradiating power of 2.0 W. (**B**) Tubular LCE coated with thick PDA layer hardly generating smoking or scorch under a low irradiating power of 1.3 W. In the tests, the samples of PDA-coated tubular LCE were suspended between two objects, and two ends of samples were fixed on the two objects.

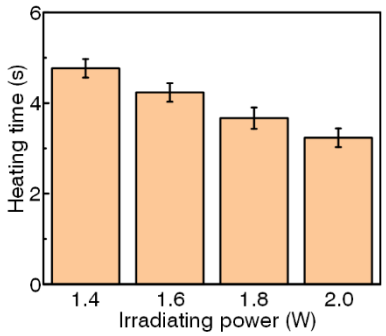

Fig. S14. Heating time of multifunctional artificial muscle under different irradiating powers. In test, the irradiating time, we defined, was heating time.

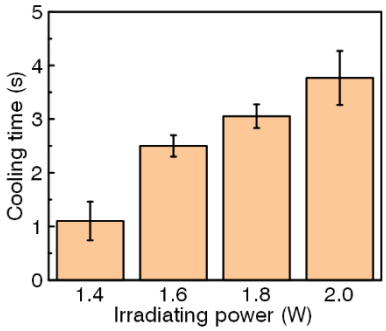

Fig. S15. Cooling time of multifunctional artificial muscle under different irradiating powers. In test, the time when the temperature decreased from the maximum to 100 ℃ (the solidifying point of LMPA) was defined as cooling time.

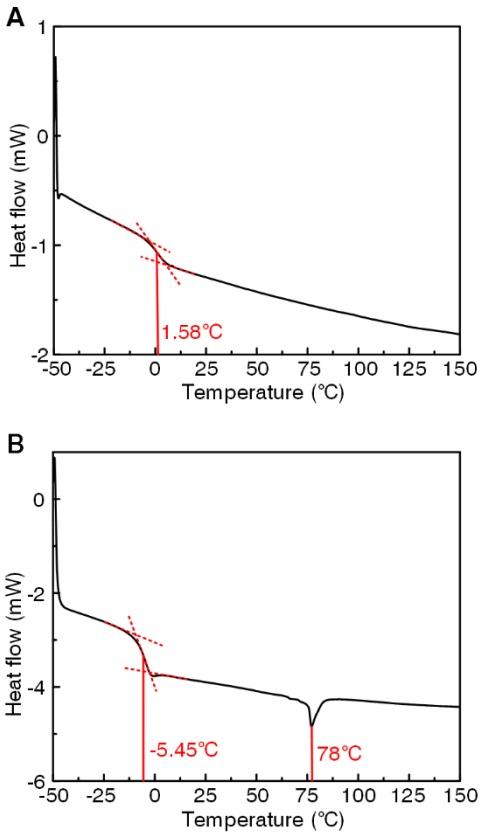

Fig. S16. Differential scanning calorimetry (DSC) curves of LCE film. (**A**) DSC curve of 2nd crosslinking LCE. (**B**) DSC curve of 1st crosslinking LCE. The glass-transition temperature of the film was obtained by calculating the position of the midpoint between the onset and offset points (two intersections of the three fitted lines, shown in red). Meanwhile, 2nd crosslinking LCE presents monodomain state and 1st crosslinking LCE presents polydomain state.

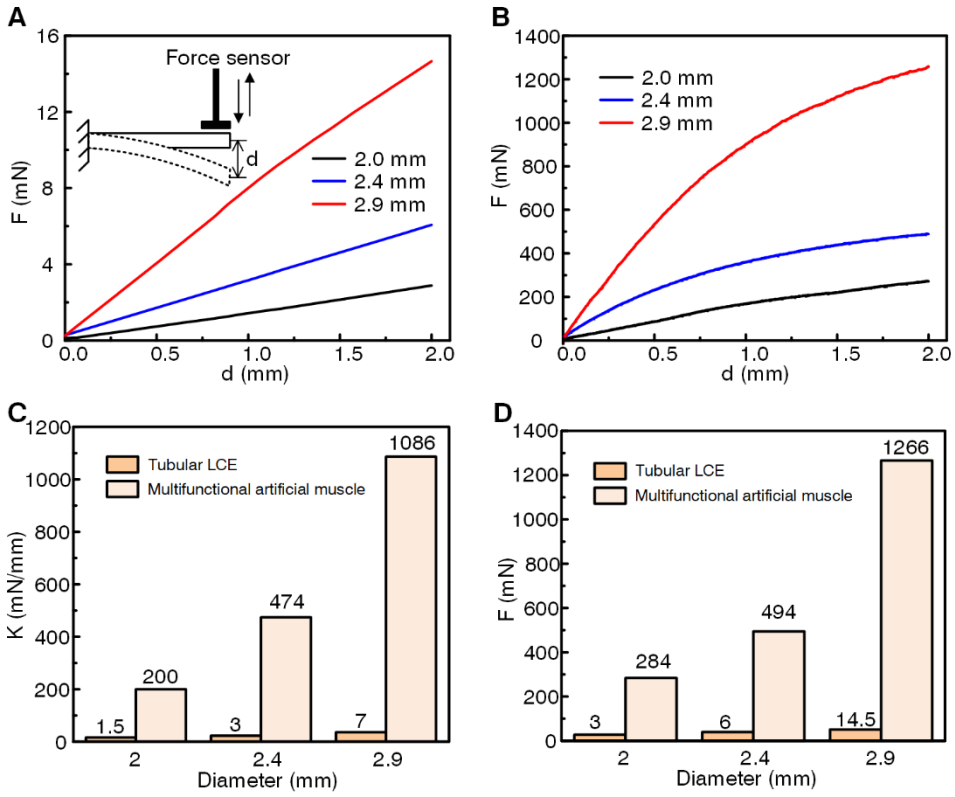

Fig. S17. Comparison of bending stiffness and load-bearing capacity of multifunctional artificial muscle and PDA-coated LCE-based tubular actuator under different outside diameters. (**A** and **B**) Output force as a function of displacement of multifunctional artificial muscle and PDA-coated LCE-based tubular actuator, respectively. (**C** and **D**) Comparison of bending stiffness and output force of multifunctional artificial muscle and PDA-coated LCE-based tubular actuator, respectively.

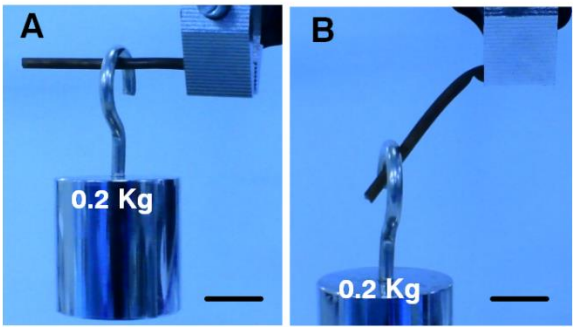

Fig. S18. Comparison of load bearing capacity of multifunctional artificial muscle and PDA-coated LCE tubular actuator. (**A**) Multifunctional artificial muscle lifting a weight of 0.2 kg. (**B**) LCE tubular actuator could not bear a weight of 0.2 kg. In (A, B), the scale bars represent 10 mm.

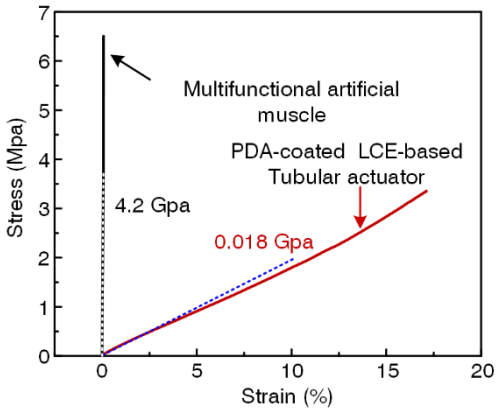

Fig. S19. Stress–strain curves of multifunctional artificial muscle and PDA-coated LCE-based tubular actuator.

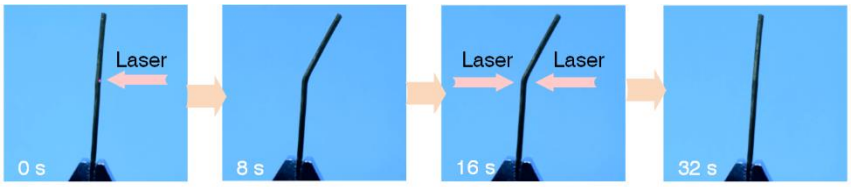

Fig. S20. **The demonstration of deformation recovery of multifunctional artificial muscle.** One end of multifunctional artificial muscle (diameter: 2.4 mm; length: 50 mm) was fixed, and the other end was free. Two laser beams of 1.3 W was applied on both sides of bending position of artificial muscle. By alternately or simultaneously irradiating the bending position, the artificial muscle finally recovered to upright state.

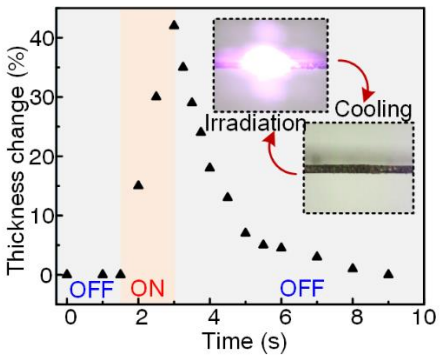

Fig. S21. The thickness change of PDA-coated LCE film under the irradiating power of 1.8 W. To quantitatively characterize the thickness change of PDA-coated LCE film before and after irradiated by laser, we defined the strain of thickness change as $\varepsilon = (h - H)/H \times 100\%$, where H and h were the thicknesses of LCE film in the initial and actuated states, respectively. When the laser was applied on the surface of LCE film at 1.5 s, the film thickened along the thickness direction. The thickness of film at the irradiating section reached the maximum value at 3 s. After the laser was turned off at 3 s, the LCE film began to recover along the thickness direction. The whole actuating process was recorded by camera (Nikon, D7500) and analyzed by ImageJ. Hence, the thickness change of LCE film could be calculated by above equation. Based on the measured data, the thickness could increase to 42% when the laser was turned off at 3 s, and the thickness change recovered to zero (i.e., original thickness) at 9 s.

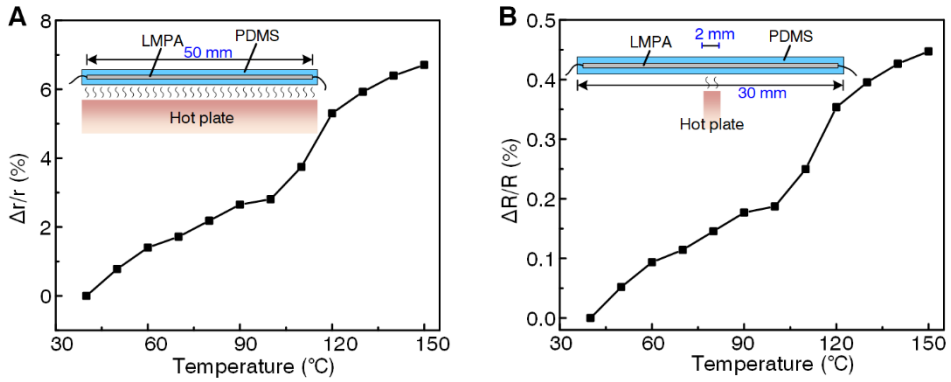

Fig. S22. Resistance change of LMPA with temperature. (**A**) Resistance-temperature curve of 30 mm-length LMPA rod that was wholly heated by hot plate in test. Δ*r/r* represents the resistance change of 30 mm-length LMPA rod. (**B**) Resistance-temperature curve of 30 mm-length LMPA rod that was only heated by 2 mm-length hot plate in ideal condition. Particularly, if the heating length of the sample was shortened to 2 mm, i.e., one fifteenth of the original length, the resistance change (*ΔR/R*) of the sample under ideal condition would also be one-fifteenth of the original value based on the equation of $\Delta R/R = \frac{\left[\frac{1}{15}\left(\frac{\Delta r}{r}\right)+\frac{14}{15}\cdot 0\right]}{1} = \frac{1}{15}(\Delta r/r)$. In the ideal condition, the resistance of LMPA that was not heated by hot plate, we assumed, was unchangeable.

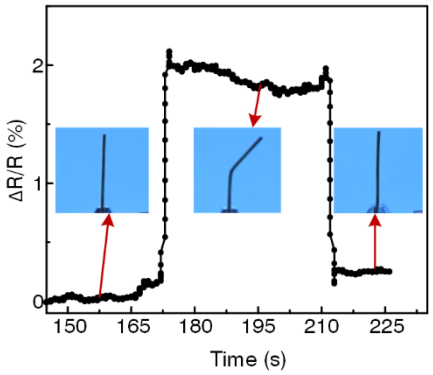

Fig. S23. Resistance change with deformation for multifunctional artificial muscle. One end of multifunctional artificial muscle (diameter: 2.4 mm; length: 50 mm) was fixed, and the other end was free. In bending process, a laser beam of 2.0 W was applied on the middle surface of the multifunctional artificial muscle. In recovery process, two laser beams of 1.3 W were applied on both sides of bending position of artificial muscle. By alternately or simultaneously irradiating the bending position, the bending behavior and resistance were monitored simultaneously.

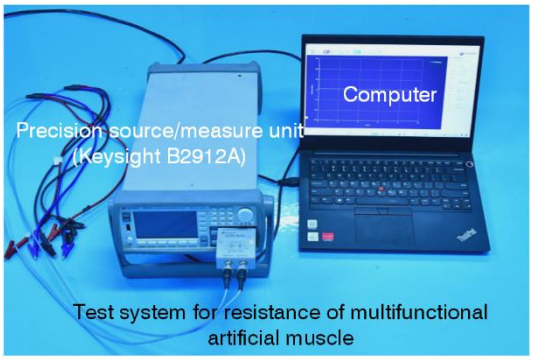

Fig. S24. Test system for resistance of multifunctional artificial muscle. Resistance data of multifunctional artificial muscle was collected by precision source/measure unit (Keysight B2912A), whose minimum measurement resolution: 10 fA/100 nV.

Table S1. Values of parameters adopted in the numerical simulations.

Parameter	Description	Value
k_1	Thermal conductivity of LCE	0.6 $Wm^{-1}K^{-1}$ (Assumed)
c_1	Specific Heat of LCE	1700 J kg^{-1} K^{-1} (Assumed)
α_1	Thermal expansion coefficient of LCE	-0.006 ~ 0 K^{-1} (measured)
h_c	Natural convection coefficient	10 $Wm^{-2}K^{-1}$ (Assumed)
ρ_1	Density of LCE	1200 Kgm^{-3} (Measured)
ν_1	Poisson's ratio of LCE	0.49 (Assumed)
E_1	Young's Modulus of LCE	0.5 MPa (Assumed)
k_2	Thermal conductivity of LMPA (Room temperature)	3.5 $Wm^{-1}K^{-1}$ (Assumed)
ρ_2	Density of LMPA	9750 Kgm^{-3} (Measured)
α_2	Thermal expansion coefficient of LMPA	5e-6 K^{-1} (Assumed)
c_2	Specific heat of LMPA	350 J kg^{-1} K^{-1} (Assumed)
ν_2	Poisson's ratio of LMPA	0.3 (Assumed)

Table S2. Values of Young's Modulus and Poisson Ratio of LMPA adopted in the numerical simulations

Young's Modulus/pa	Poisson's Ratio	Temperature/°C
100000000	0.3	20
10000000	0.3	30
1000000	0.3	50
300000	0.3	80
1	0.3	180
1	0.3	300
1	0.3	500

Table S3. Values of Young's Modulus and Poisson Ratio of LCE adopted in the numerical simulations.

Young's Modulus/pa	Poisson's Ratio	Temperature/°C
500000	0.49	20
500000	0.49	30
500000	0.49	50
500000	0.49	80
500000	0.49	180
500000	0.49	300
500000	0.49	500

Movie S1. Deformation locking property of multifunctional artificial muscle (1×).

Movie S2. Reversible bending deformation of PDA-coated LCE-based tubular actuator (1×).

Movie S3. The stress distribution of multifunctional artificial muscle under the irradiating power of 2.0 W in simulation (0.2×).

Movie S4. The temperature distribution of multifunctional artificial muscle under the irradiating power of 2.0 W in simulation (0.2×).

Movie S5. Bending angle of multifunctional artificial muscle can be increased by increasing irradiating time (1×).

Movie S6. Bending direction of multifunctional artificial muscle can be adjusted by changing laser irradiating direction (3×).

Movie S7. Demonstration of multifunctional artificial muscle possessing any number of bending joints (3×).

Movie S8. Demonstration of complicated shape of multifunctional artificial muscle by irradiating different positions and from different directions (1×).

Movie S9. Shape transformation of multifunctional artificial muscle under the irradiating power of 1.2 W (1×).

Movie S10. Demonstration of deformation locking property of multifunctional artificial muscle with the melting point of 47 ℃ (1×).

Movie S11. Demonstration of deformation locking property of multifunctional artificial muscle with the melting point of 82 ℃ (1×).

Movie S12. Demonstration of deformation locking property of multifunctional artificial muscle with the melting point of 100 ℃ (1×).

Movie S13. Demonstration of the multifunctional artificial muscle lifting and carrying a 100-g object assisted by a robot arm (3×).

Movie S14. Demonstration of deformation recovery of multifunctional artificial muscle (3×).

Movie S15. The thickness change of PDA-coated LCE film under light stimuli (1×).

REFERENCES AND NOTES

1. A. Billard, D. Kragic, Trends and challenges in robot manipulation. *Science* **364**, 1149 (2019).

2. G.-Z. Yang, J. Bellingham, P. E. Dupont, P. Fischer, L. Floridi, R. Full, N. Jacobstein, V. Kumar, M. McNutt, R. Merrifield, B. J. Nelson, B. Scassellati, M. Taddeo, R. Taylor, M. Veloso, Z. L. Wang, R. Wood, The grand challenges of *Science Robotics*. *Sci. Robot.* **3**, eaar7650 (2018).

3. B. A. Trimmer, Metal or muscle? The future of biologically inspired robots. *Sci. Robot.* **5**, eaba6149 (2020).

4. D. X. Ba, H. Yeom, J. Bae, A direct robust nonsingular terminal sliding mode controller based on an adaptive time-delay estimator for servomotor rigid robots. *Mechatronics* **59**, 82–94 (2019).

5. F. Flacco, A. De Luca, O. Khatib, Control of redundant robots under hard joint constraints: Saturation in the null space. *IEEE Trans. Robot.* **31**, 637–654 (2015).

6. M. Cestari, D. Sanz-Merodio, E. Garcia, A new and versatile adjustable rigidity actuator with add-on locking mechanism (ARES-XL). *Actuators* **7**, 1–21 (2018).

7. C. J. Payne, I. Wamala, D. Bautista-Salinas, M. Saeed, D. V. Story, T. Thalhofer, M. A. Horvath, C. Abah, P. J. del Nido, C. J. Walsh, N. V. Vasilyev, Soft robotic ventricular assist device with septal bracing for therapy of heart failure. *Sci. Robot.* **2**, eaan6736 (2017).

8. Y. Kim, G. A. Parada, S. Liu, X. Zhao, Ferromagnetic soft continuum robots. *Sci. Robot.* **4**, eaax7329 (2019).

9. X. Liu, Y. Yang, M. E. Inda, S. Lin, J. Wu, Y. Kim, X. Chen, D. Ma, T. K. Lu, X. Zhao, Magnetic living hydrogels for intestinal localization, retention, and diagnosis. *Adv. Funct. Mater.* **31**, 2010918 (2021).

10. E. T. Roche, M. A. Horvath, I. Wamala, A. Alazmani, S.-E. Song, W. Whyte, Z. Machaidze, C. J. Payne, J. C. Weaver, G. Fishbein, J. Kuebler, N. V. Vasilyev, D. J. Mooney, F. A. Pigula, C. J. Walsh, Soft robotic sleeve supports heart function. *Sci. Transl. Med.* **9**, eaaf3925 (2017).

11. Y. Roh, M. Kim, S. M. Won, D. Lim, I. Hong, S. Lee, T. Kim, C. Kim, D. Lee, S. Im, G. Lee, D. Kim, D. Shin, D. Gong, B. Kim, S. Kim, S. Kim, H. K. Kim, B.-K. Koo, S. Seo, J.-S. Koh, D. Kang, S. Han, Vital signal sensing and manipulation of a microscale organ with a multifunctional soft gripper. *Sci. Robot.* **6**, eabi6774 (2021).

12. G. Gu , J. Zou, R. Zhao, X. Zhao, X. Zhu, Soft wall-climbing robots. *Sci. Robot.* **3**, eaat2874 (2018).

13. J. Huang, Y. Liu, Y. Yang, Z. Zhou, J. Mao, T. Wu, J. Liu, Q. Cai, C. Peng, Y. Xu, B. Zeng, W. Luo, G. Chen, C. Yuan, L. Dai, Electrically programmable adhesive hydrogels for climbing robots. *Sci. Robot.* **6**, eabe1858 (2021).

14. B. Shin, J. Ha, M. Lee, K. Park, G. H. Park, T. H. Choi, K.-J. Cho, H.-Y. Kim, Hygrobot: A self-locomotive ratcheted actuator powered by environmental humidity. *Sci. Robot.* **3**, eaar2629 (2018).

15. W. Hu, G. Z. Lum, M. Mastrangeli, M. Sitti, Small-scale soft-bodied robot with multimodal locomotion. *Nature* **554**, 81–85 (2018).

16. T. Xu, J. Zhang, M. Salehizadeh, O. Onaizah, E. Diller, Millimeter-scale flexible robots with programmable three-dimensional magnetization and motions. *Sci. Robot.* **4**, eaav4494 (2019).

17. J. Mu, M. J. Andrade, S. Fang, X. Wang, E. Gao, N. Li, S. H. Kim, H. Wang, C. Hou, Q. Zhang, M. Zhu, D. Qian, H. Lu, D. Kongahage, S. Talebian, J. Foroughi, G. Spinks, H. Kim, T. H. Ware, H. J. Sim, D. Y. Lee, Y. Jang, S. J. Kim, R. H. Baughman, Sheath-run artificial muscles. *Science* **365**, 150–155 (2019).

18. F. Zhai, Y. Feng, Z. Li, Y. Xie, J. Ge, H. Wang, W. Qiu, W. Feng, 4D-printed untethered self-propelling soft robot with tactile perception: Rolling, racing, and exploring. *Matter* **4**, 3313–3326 (2021).

19. S. Li, D. M. Vogt, D. Rus, R. J. Wood, Fluid-driven origami-inspired artificial muscles. *Proc. Natl. Acad. Sci. U.S.A.* **114**, 13132–13137 (2017).

20. C. Christianson, N. N. Goldberg, D. D. Deheyn, S. Cai, M. T. Tolley, Translucent soft robots driven by frameless fluid electrode dielectric elastomer actuators. *Sci. Robot.* **3**, eaat1893 (2018).

21. C. Ahn, X. Liang, S. Cai, Bioinspired design of light-powered crawling, squeezing, and jumping untethered soft robot. *Adv. Mater. Technol.* **4**, 1900185 (2019).

22. Y. Chen, H. Zhao, J. Mao, P. Chirarattananon, E. F. Helbling, N. P. Hyun, D. R. Clarke, R. J. Wood, Controlled flight of a microrobot powered by soft artificial muscles. *Nature* **575**, 324–329 (2019).

23. H. Fu, K. Nan, W. Bai, W. Huang, K. Bai, L. Lu, C. Zhou, Y. Liu, F. Liu, J. Wang, M. Han, Z. Yan, H. Luan, Y. Zhang, Y. Zhang, J. Zhao, X. Cheng, M. Li, J. W. Lee, Y. Liu, D. Fang, X. Li, Y. Huang, Y. Zhang, J. A. Rogers, Morphable 3D mesostructures and microelectronic devices by multistable buckling mechanics. *Nat. Mater.* **17**, 268–276 (2018).

24. L. Puig, A. Barton, N. Rando, A review on large deployable structures for astrophysics missions. *Acta Astronaut.* **67**, 12–26 (2010).

25. Q. Ze, X. Kuang, S. Wu, J. Wong, S. M. Montgomery, R. Zhang, J. M. Kovitz, F. Yang, H. J. Qi, R. Zhao, Magnetic shape memory polymers with integrated multifunctional shape manipulation. *Adv. Mater.* **32**, 1906657 (2020).

26. S. Park, H. Yuk, R. Zhao, Y. S. Yim, E. W. Woldeghebriel, J. Kang, A. Canales, Y. Fink, G. B. Choi, X. Zhao, P. Anikeeva, Adaptive and multifunctional hydrogel hybrid probes for long-term sensing and modulation of neural activity. *Nat. Commun.* **12**, 3435 (2021).

27. J. Chen, K. Han, J. Luo, L. Xu, W. Tang, Z. L. Wang, Soft robots with self-powered configurational sensing. *Nano Energy* **77**, 105171 (2020).

28. Y. F. Zhang, N. Zhang, H. Hingorani, N. Ding, D. Wang, C. Yuan, B. Zhang, G. Gu, Q. Ge, Fast-response, stiffness-tunable soft actuator by hybrid multimaterial 3D printing. *Adv. Funct. Mater.* **29**, 1806698 (2019).

29. S. Zhuo, Z. Zhao, Z. Xie, Y. Hao, Y. Xu, T. Zhao, H. Li, E. M. Knubben, L. Wen, L. Jiang, M. Liu, Complex multiphase organohydrogels with programmable mechanics toward adaptive soft-matter machines. *Sci. Adv.* **6**, eaax1464 (2020).

30. A. Tonazzini, S. Mintchev, B. Schubert, B. Mazzolai, J. Shintake, D. Floreano, Variable stiffness fiber with self-healing capability. *Adv. Mater.* **28**, 10142–10148 (2016).

31. A. Kotikian, J. M. Morales, A. Lu, J. Mueller, Z. S. Davidson, J. W. Boley, J. A. Lewis, Innervated, self-sensing liquid crystal elastomer actuators with closed loop control. *Adv. Mater.* **33**, 2101814 (2021).

32. M. J. Ford, C. P. Ambulo, T. A. Kent, E. J. Markvicka, C. Pan, J. Malen, T. H. Ware, C. Majidi, A multifunctional shape-morphing elastomer with liquid metal inclusions. *Proc. Natl. Acad. Sci. U.S.A.* **116**, 21438–21444 (2019).

33. L. Yu, R. Peng, G. Rivers, C. Zhang, P. Si, B. Zhao, Multifunctional liquid crystal polymer network soft actuators. *J. Mater. Chem. A* **8**, 3390–3396 (2020).

34. Y. Zhao, C.-Y. Lo, L. Ruan, C.-H. Pi, C. Kim, Y. Alsaid, I. Frenkel, R. Rico, T.-C. Tsao, X. He, Somatosensory actuator based on stretchable conductive photothermally responsive hydrogel. *Sci. Robot.* **6**, eabd5483 (2021).

35. G. H. F. Bergmann, H. Finkelmann, Liquid-crystalline main-chain elastomers. *Macromol. Rapid Commun.* **18**, 353–360 (1997).

36. C. M. Yakacki, M. Saed, D. P. Nair, T. Gong, S. M. Reed, C. N. Bowman, Tailorable and programmable liquid-crystalline elastomers using a two-stage thiol–acrylate reaction. *RSC Adv.* **5**, 18997–19001 (2015).

37. A. Kotikian, R. L. Truby, J. W. Boley, T. J. White, J. A. Lewis, 3D Printing of liquid crystal elastomeric actuators with spatially programed nematic order. *Adv. Mater.* **30**, 1706164 (2018).

38. A. H. Gelebart, M. Mc Bride, A. P. H. J. Schenning, C. N. Bowman, D. J. Broer, Photoresponsive fiber array: Toward mimicking the collective motion of cilia for transport applications. *Adv. Funct. Mater.* **26**, 5322–5327 (2016).

39. A. S. Kuenstler, H. Kim, R. C. Hayward, Liquid crystal elastomer waveguide actuators. *Adv. Mater.* **31**, 1901216 (2019).

40. Y. Liu, K. Ai, J. Liu, M. Deng, Y. He, L. Lu, Dopamine-melanin colloidal nanospheres: An efficient near-infrared photothermal therapeutic agent for in vivo cancer therapy. *Adv. Mater.* **25**, 1353–1359 (2013).

41. Z. Li, Y. Yang, Z. Wang, X. Zhang, Q. Chen, X. Qian, N. Liu, Y. Wei, Y. Ji, Polydopamine nanoparticles doped in liquid crystal elastomers for producing dynamic 3D structures. *J. Mater. Chem. A* **5**, 6740–6746 (2017).

42. L. Li, B. Xue, C. Zhang, Y. Geng, X. Pan, Q. Zhang, Thermal effect analysis of continuous laser assisted hot machining alumina ceramics. *Laser Infrared* **50**, 1 (2020).

43. Z. Zhou, H. Yi, Discuss the calculating formula of moment of inertia for bow-shaped test piece in GB/T 13096.2–91. *Fiber Reinf. Plast. Comp.* **1**, 3 (2001).

44. Y. Yang, Y. Chen, Y. Li, Z. Wang, Y. Li, Novel variable-stiffness robotic fingers with built-in position feedback. *Soft Robot.* **4**, 338–352 (2017).

45. Y. Yang, Y. Chen, Y. Wei, Y. Li, Novel design and three-dimensional printing of variable stiffness robotic grippers. *J. Mech. Robot.* **8**, 061010 (2016).

46. Y. Yang, Y. Chen, Y. Li, M. Z. Q. Chen, Y. Wei, Bioinspired robotic fingers based on pneumatic actuator and 3D printing of smart material. *Soft Robot.* **4**, 147–162 (2017).

47. Z. Wang, Z. Wang, Y. Zheng, Q. He, Y. Wang, S. Cai, Three-dimensional printing of functionally graded liquid crystal elastomer. *Sci. Adv.* **6**, eabc0034 (2020).

48. Y. Li, H. Yu, K. Yu, X. Guo, X. Wang, Reconfigurable three-dimensional mesotructures of spatially programmed liquid crystal elastomers and their ferromagnetic composites. *Adv. Funct. Mater.* **31**, 2100338 (2021).

49. K. Liu, F. Hacker, C. Daraio, Robotic surfaces with reversible, spatiotemporal control for shape morphing and object manipulation. *Sci. Robot.* **6**, eabf5116 (2021).

50. H. Tian, Z. Wang, Y. Chen, J. Shao, T. Gao, S. Cai, Polydopamine-coated main-chain liquid crystal elastomer as optically driven artificial muscle. *ACS Appl. Mater. Interfaces* **10**, 8307–8316 (2018).

51. J. Gibson, X. Liu, S. V. Georgakopoulos, T. Ware, J. J. Wie, T. J. White, Novel reconfigurable antennas using liquid crystals elastomers, in *Proceedings of the 2015 IEEE International Symposium on Antennas and Propagation & USNC/URSI National Radio Science Meeting* (IEEE, 2015), pp. 2297–2298.

52. Y.-G. Park, H. S. An, J.-Y. Kim, J.-U. Park, High-resolution, reconfigurable printing of liquid metals with three-dimensional structures. *Sci. Adv.* **5**, eaaw2844 (2019).

53. S. I. H. Shah, S. Lim, Thermally beam-direction- and beamwidth-switchable monopole antenna using origami reflectors with smart shape memory polymer hinges. *IEEE Antennas Wirel. Propag. Lett.* **18**, 1696–1700 (2019).

54. H. Liu, H. Tian, J. Shao, Z. Wang, X. Li, C. Wang, X. Chen, An electrically actuated soft artificial muscle based on a high-performance flexible electrothermal film and liquid-crystal elastomer. *ACS Appl. Mater. Interfaces* **12**, 56338–56349 (2020).

55. B. E. Schubert, D. Floreano, Variable stiffness material based on rigid low-melting-point-alloy microstructures embedded in soft poly(dimethylsiloxane) (PDMS). *RSC Adv.* **3**, 24671 (2013).

56. S. M. Mirvakili, I. W. Hunter, Artificial muscles: Mechanisms, applications, and challenges. *Adv. Mater.* **30**, 1704407 (2018).

57. K. C. Galloway, Y. Chen, E. Templeton, B. Rife, I. S. Godage, E. J. Barth, Fiber optic shape sensing for soft robotics. *Soft Robot.* **6**, 671–684 (2019).

58. B. Oh, Y.-G. Park, H. Jung, S. Ji, W. H. Cheong, J. Cheon, W. Lee, J.-U. Park, Untethered soft robotics with fully integrated wireless sensing and actuating systems for somatosensory and respiratory functions. *Soft Robot.* **7**, 564–573 (2020).

59. T. G. Thuruthel, B. Shih, C. Laschi, M. T. Tolley, Soft robot perception using embedded soft sensors and recurrent neural networks. *Sci. Robot.* **4**, eaav1488 (2019).

60. I. M. Van Meerbeek, C. M. De Sa, R. F. Shepherd, Soft optoelectronic sensory foams with proprioception. *Sci. Robot.* **3**, eaau2489 (2018).

61. L. Ma, Q. Li, Re-discussion of the calculating formula of moment of inertia for bow-shaped test piece in GB/T 13096.2–1991. *Fiber Composites* **1**, 32 (2009).